Journal of Materials Chemistry A

ROYAL SOCIETY OF CHEMISTRY

PAPER

View Article Online
View Journal

Cite this: DOI: 10.1039/d5ta10043g

Ligand-substituted inorganic–organic hybrid materials for efficient urea-assisted electrocatalytic water splitting

Lingshen Meng, †[a] Zeyi Zhang,†[a] Carlos A. Triana, *[a] Aaron A. Schultz,[a] Hang Chen, [a] Dan Zhang[b] and Greta R. Patzke *[a]

Received 8th December 2025
Accepted 8th March 2026

DOI: 10.1039/d5ta10043g

rsc.li/materials-a

Strategies for the structural tuning of inorganic–organic hybrid materials are crucial for their technological application. We present a ligand replacement strategy for NiClOH–Pm_xPz_{1-x} inorganic–organic hybrid nanorods (Pm = pyrimidine, Pz = pyrazine) to improve their performance in urea-assisted water splitting. Through partial substitution of pyrimidine ligands with pyrazines, oxygen vacancies were introduced into initially synthesized NiClOH–Pm nanorods. The NiClOH–Pm_xPz_{1-x} composite material exhibits excellent performance in electrocatalytic urea oxidation, with a higher electrochemical double layer capacitance (23.8 mF cm^{-2}) and a rather small Tafel slope (41.9 mV dec^{-1}) compared to most previous reports, reaching potentials of 1.37 and 1.53 V at 10 mA cm^{-2} and 100 mA cm^{-2}, respectively. The optimized ligand ratio (Pm/Pz = 33/1) enhances π–π interactions, which improves electron transfer between ligands and Ni centers, and thereby the catalytic efficiency. DFT calculations show that the adsorption of urea molecules on Ni centers takes precedence over the adsorption of OH^- during the electrocatalytic process. This work offers a design strategy to improve the electrochemical performance of hybrid inorganic–organic materials through substitutional ligand design.

Introduction

Electrochemical water splitting, proceeding through the hydrogen evolution reaction (HER) at the cathode and the oxygen evolution reaction (OER) at the anode, has attracted significant attention as a promising approach to store solar energy in the form of renewable fuels.[1–4] However, the high thermodynamic potential (1.23 V *vs.* RHE) required for the OER limits the overall efficiency of the water splitting process. In contrast, the urea oxidation reaction (UOR), with a much lower theoretical potential (0.37 V *vs.* RHE), has emerged as an alternative anode reaction for achieving more efficient electrochemical hydrogen production.[5] Ni-based materials, including oxides,[6,7] sulfides,[8,9] phosphides,[10,11] alloys,[12,13] and others,[14–17] are among the most active non-precious metal catalysts for the UOR. To fully exploit their catalytic potential, the electronic structure and coordination environment around Ni centers must be precisely tuned.[18,19] This is crucial not only for enabling the transformation of Ni species from their as-synthesized state into active, high-valent intermediates (such as NiOOH) but also for ensuring that these intermediates effectively adsorb and interact with urea.[20–22]

In previous studies, multiple strategies such as defect[18,23] or interface engineering,[24,25] heteroatom doping,[26–29] and the development of atomically dispersed Ni active sites[30,31] have been explored to optimize Ni-based catalysts. Recently, organic ligand modification in organic–inorganic hybrid materials has emerged as a controllable and versatile route for precise electrocatalyst design.[32–34] In contrast to direct modification of the inorganic phases, the ligand substitution method mainly targets the organic ligands, while leaving the inorganic framework largely unchanged.[34] This provides a quite versatile approach to constructing complex, asymmetric organic–inorganic hybrid materials. The π–π interactions between different ligands allow for more efficient electron migration, thereby enhancing the electrocatalytic performance.[35] Inorganic–organic hybrid materials have demonstrated promising UOR performance through exploiting the tunable coordination environment offered by organic ligands around the active Ni sites.[36] Tuning the coordination environment and electronic properties of Ni centers with organic ligand modifications enables fine control over the catalytic behaviour and leads to high efficiency in UOR electrocatalysis.[34] Gong and co-workers, for example, used $NiCl_2$ and pyrazine to prepare an organic–inorganic hybrid material (NiHC–Pz). Then, by partial ligand removal *via* vacuum heating, they introduced some ligand-vacancies in the materials, resulting in a highly active UOR electrocatalyst.[34]

Incorporating N-based organic ligands has emerged as an effective method to stabilize NiOOH intermediates.[37] Compared

[a]*Department of Chemistry, University of Zurich, CH-8057 Zurich, Switzerland. E-mail: carlos.triana@chem.uzh.ch; greta.patzke@chem.uzh.ch*

[b]*Institute of Photochemistry and Photofunctional Materials, University of Shanghai for Science and Technology, Shanghai 20093, China*

† These authors contributed equally: Lingshen Meng and Zeyi Zhang.

to hydroxide ions and oxygen-containing organic ligands, N-based ligands possess lower electronegativity, which increases the electron density around the Ni centers. The increased electron density around Ni centers suppresses further oxidation to high-valence states ($Ni^{3+\delta}O_xH_y$), which would be more beneficial for the competing OER than for the UOR. This electronic effect helps to maintain Ni in the oxidation states (NiOOH) that are considered catalytically competent for UOR, thereby improving the selectivity towards the UOR in favor of the OER and the overall reactivity. In addition, the π-conjugated structures of many N-containing ligands facilitate metal–ligand orbital interactions, which contribute to improved charge-transport properties in hybrid materials.[38] N-containing bidentate ligands featuring two N coordination sites (hereafter referred to as dual N ligands) exhibit rich π-electron conjugation and tunable coordination environments. Some ligands with two nitrogen centers, such as pyrimidine, pyrazine, pyridazine, bipyridine, and phenanthroline, contain π-electron systems that can facilitate π–π stacking interactions, further enhancing the electrical conductivity of the resulting hybrid material.[39] Their structural flexibility and electronic features allow precise control over Ni coordination environments, offering opportunities to boost UOR performance and to extend these hybrids toward more complex electrocatalytic reactions, such as biomass oxidation.

Inspired by this concept, we employed ligand substitution strategies to synthesize $Ni(OH)_2$-based inorganic–organic hybrid structures and explored their electrocatalytic properties. NiClOH–$Pm_{0.8}Pz_{0.2}$ was used as a model system to demonstrate that adjusting the structure and π–π interactions in Ni-based inorganic–organic hybrid materials by substituting pyrimidine (Pm) with pyrazine (Pz) ligands is an effective strategy to design highly active UOR electrocatalysts. We show that the introduction of pyrazine ligands modifies the coordination environment of Ni centers, and that the π–π interactions between pyrimidine and pyrazine ligands increase the electron density around them. Experimental evidence and density functional theory (DFT) calculations confirm that the ligand substitution strategy with pyrazine enhances the UOR activity through a reconstructed active intermediate containing NiOOH layers and Pm/Pz ligands. This PmPz-modified NiOOH intermediate offers stronger urea adsorption, and a higher density of Ni-d/O-p states near the Fermi level, collectively accelerating the key steps of UOR. The applied ligand substitution strategy opens up new ways to control the electron density around Ni centers for designing highly efficient UOR electrocatalysts.

Results and discussion

Synthesis and characterization of NiClOH–PmPz electrocatalysts

NiClOH–Pm, NiClOH–Pz and NiClOH–Pm_xPz_y pre-catalysts were both synthesized using a solvothermal method at 120 °C in a solution of 20 mL *N*,*N*-dimethylformamide (DMF) and 1 mL H_2O (Fig. 1 and S1), using H_2O as source of –OH groups required for hybrid formation (see Experimental section in the SI). The powder X-ray diffraction (PXRD) pattern of NiClOH–Pm shows sharp diffraction peaks at 2θ angles of 12.71°, 14.74°, 18.15°, 19.66°, 23.76°, and 26.06°, which corresponds with reference data for $NiCl_2$–pyrimidine (Fig. 2a; space group *Pmma*).[40] NiClOH–Pm adopts the orthorhombic structure motif of $NiCl_2$–pyrazine (space group *Cmmm*).[41] Different ratios of pyrazine were then substituted into NiClOH–Pm using a hydrothermal process (Experimental section S1.3 in the SI). Rietveld refinement of the powder XRD pattern of NiClOH–$Pm_{0.8}Pz_{0.2}$ yielded lattice parameters of a = 3.5076(2) Å, b = 11.9543(5) Å, c = 7.0502(3) Å, and a unit cell volume of V = 295.62(5) $Å^3$. Compared with the experimental data for NiClOH–Pm (a = 3.4991(3) Å, b = 11.9714(1) Å, c = 7.0302(1) Å, and V = 294.82(6) $Å^3$),[40] this indicates a slight expansion of the NiClOH–Pm framework upon partial substitution with Pz ligands.

X-ray photoelectron spectroscopy (XPS) was used to determine the valence states and electronic structure of NiClOH–Pm and NiClOH–$Pm_{0.8}Pz_{0.2}$ (Fig. 3a). The Ni^{2+} $2p_{3/2}$ peaks of NiClOH–Pm and NiClOH–$Pm_{0.8}Pz_{0.2}$ were detected at a binding energy of 856.6 and 858.4 eV, respectively. The slight blue shift suggests that introducing Pz creates a more asymmetric coordination environment around the Ni centers, facilitating the formation of partially undercoordinated surface Ni sites.[34,42] For the regions where lattice distortion is induced by ligand substitution, the π–π interactions between the layers are enhanced, thereby further stabilizing the Ni atoms within and leading to a slight increase in their binding energy. However, due to the structural similarities between pyrimidine and

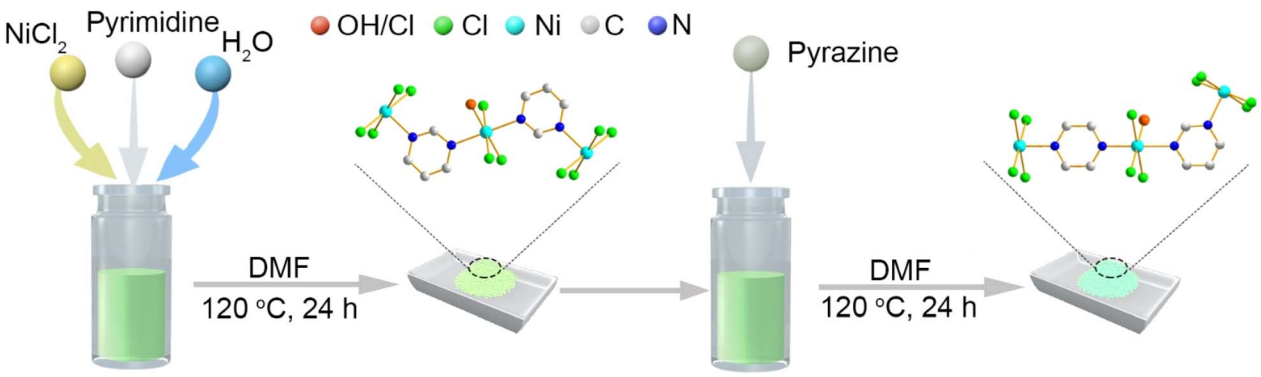

Fig. 1 Schematic illustration of the synthesis and structures of NiClOH–Pm (left) and NiClOH–Pm_xPz_{1-x} (right).

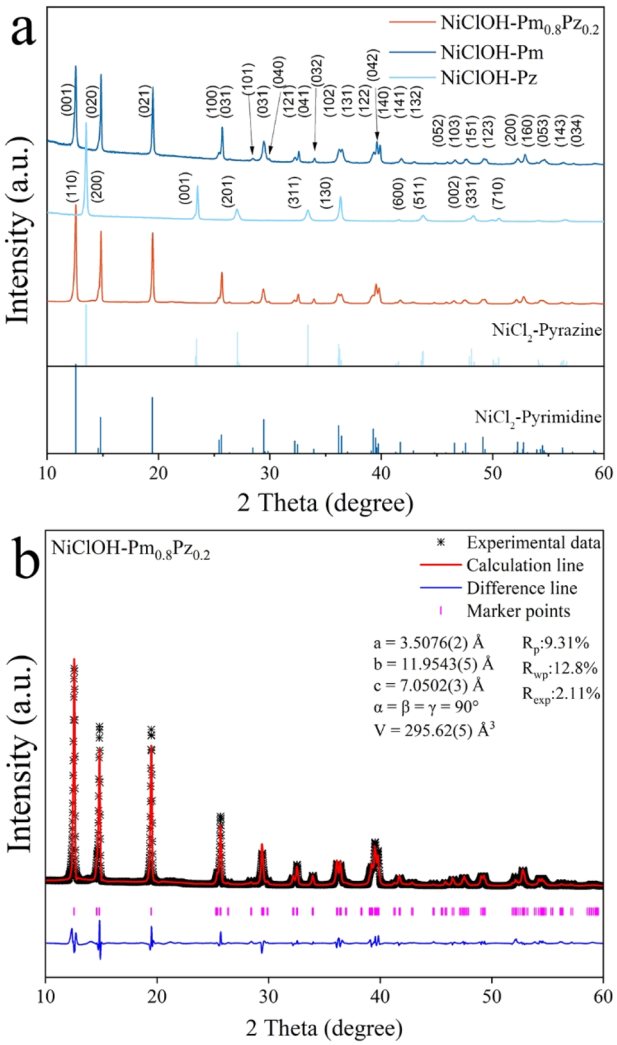

Fig. 2 (a) PXRD patterns of NiClOH–Pz, NiClOH–Pm and NiClOH–$Pm_{0.8}Pz_{0.2}$; (b) Rietveld refinement results for NiClOH–$Pm_{0.8}Pz_{0.2}$.

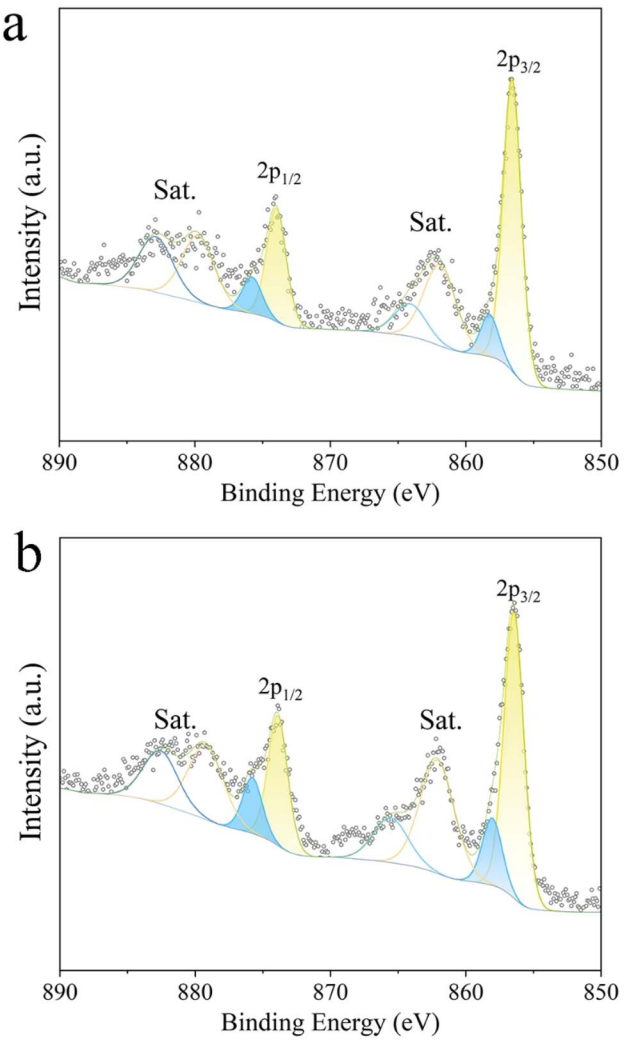

Fig. 3 Ni 2p XP spectra of (a) NiClOH–Pm and (b) NiClOH–$Pm_{0.8}Pz_{0.2}$.

pyrazine, the increase in binding energy is relatively small.[43,44] In order to compare the areas between the peaks more accurately, the full width at half maximum (FWHM) was kept constant during the fitting process to ensure the reliability of the fitting results. However, from 0 to 0.2 equivalents of ligand replacement, the Ni^{2+} peak area in the sample NiClOH–$Pm_{0.8}Pz_{0.2}$ increased from ~79% to ~86%. This indicates that ligand replacement changes both electronic structure and coordination environments.[45] Very low amounts of Ni^{3+} might be attributed to surface oxidation. For Cl $2p_{1/2}$, the binding energy shifts from 198.2 in NiClOH–Pm to 198.6 in NiClOH–$Pm_{0.8}Pz_{0.2}$, suggesting a decrease in the electron density around Cl, implying a shift from Cl to Ni centers. NiClOH–Pm displayed one strong O 1s signal at 532.1 eV for –OH in the hybrid material (Fig. S2)[46] and another signal at 534.0 eV assigned to surface absorbed O species. The positions of the corresponding two peaks of NiClOH–$Pm_{0.8}Pz_{0.2}$ were shifted to higher energies at 532.5 and 534.5 eV, respectively. The type and relative amounts of oxygen species are consistent with the results obtained from TGA analyses (discussed below). Ligand substitution resulted in a progressive increase in the binding energy of the O 1s peaks, most notably for the –OH component.

X-ray absorption spectroscopy (XAS) measurements were conducted to investigate the electronic structure and local coordination environment of Ni atoms in NiClOH–Pm and NiClOH–$Pm_{0.8}Pz_{0.2}$ samples (Fig. 4a–c). The energy positions of the main absorption edge in the X-ray absorption near-edge structure (XANES) spectrum of NiClOH–$Pm_{0.8}Pz_{0.2}$ and NiClOH–Pm, respectively, are quite close to the $Ni(OH)_2$ reference (Fig. 4a). The extended X-ray absorption fine structure (EXAFS) spectra of pristine NiClOH–Pm and NiClOH–$Pm_{0.8}Pz_{0.2}$ show a main peak at 2.34 Å arising from backscattering from first and second shell coordinated N and Cl atoms at bond distances of Ni–N = 2.06 Å and Ni–Cl = 2.39 Å for NiClOH–Pm and Ni–N = 2.04 Å and Ni–Cl = 2.39 Å for NiClOH–$Pm_{0.8}Pz_{0.2}$, respectively (Fig. 4a–c and Table S1).

Thermogravimetric analysis (TGA) of NiClOH–Pm, depicted in Fig. S3, shows three significant mass loss steps: the initial drop until at approximately 270 °C, accounting for about 23% of the total mass, was attributed to water evaporation. The subsequent mass reduction in the range of 360 to 450 °C,

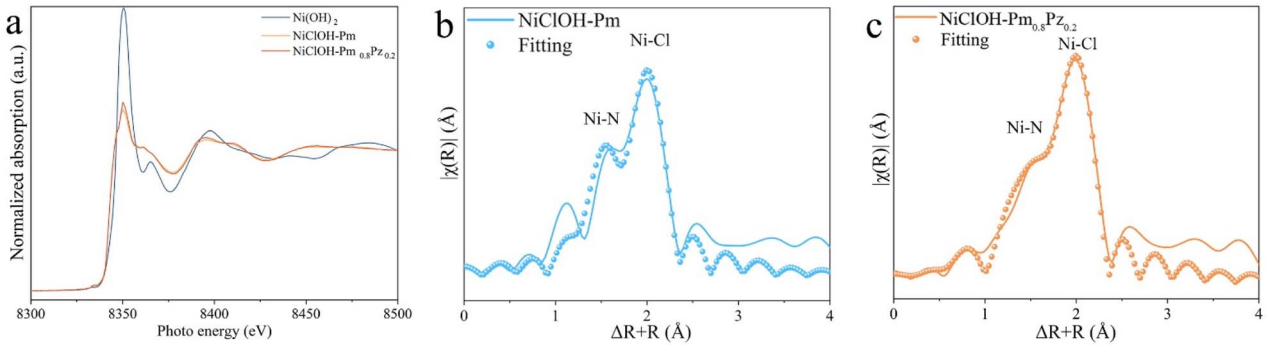

Fig. 4 (a) XANES of $Ni(OH)_2$, NiClOH–Pm and NiClOH–$Pm_{0.8}Pz_{0.2}$; (b and c) EXAFS spectra and fitting results of NiClOH–Pm and NiClOH–$Pm_{0.8}Pz_{0.2}$.

representing roughly 30% of the initial mass, corresponds to the evaporation of both pyrimidine and pyrazine due to their similar boiling points of 123 and 115 °C, respectively. The mass loss temperature shown in the TGA curve is significantly higher than the intrinsic boiling point/decomposition temperature of the ligand molecules, which is mainly attributed to their Ni–N coordination, which improves the thermal stability of the ligand. Another mass loss step of about 27% near 710 °C was detected, which likely results from the decomposition of the $NiCl_2$ in NiClOH–$Pm_{0.8}Pz_{0.2}$ and evaporation of HCl.[34]

The morphology and elemental composition of the hybrid materials were examined by transmission electron microscopy (TEM), scanning electron microscopy (SEM), and energy-dispersive X-ray spectroscopy (EDX). TEM images, as depicted in Fig. S4a and b, show that the hybrid materials display a nanorod morphology, which was retained after ligand exchange, in line with SEM images (Fig. S4c–e). EDX mappings (Fig. S4c) revealed a homogeneous distribution of C, N, O, Cl and Ni on the sample surfaces. EDX spot analyses provided a first insight into the stoichiometry of the hybrid materials, revealing a Ni : Cl molar ratio of approximately 1 : 1.11 which agrees with the nominal ratio of 1 : 1. Inductively coupled plasma mass spectrometry (ICP-MS) was employed to confirm the concentration of Ni and Cl (Table S4), and the results agree with EDX analyses. BET surface area analysis was employed to determine the surface area of NiClOH–$Pm_{0.8}Pz_{0.2}$ and other hybrid materials. As shown in Fig. S5, the surface areas of NiClOH–Pm and NiClOH–Pz were determined as 26.4 and 27.1 $m^2\ g^{-1}$, respectively, which is in the range of NiClOH–$Pm_{0.8}Pz_{0.2}$ (27.4 $m^2\ g^{-1}$).

To confirm that Pm was successfully replaced by Pz, Fourier-transform infrared spectroscopy (FT-IR) and ^1H nuclear magnetic resonance (^1H NMR) spectroscopy were used to monitor the changes in the chemical bonding of the samples for different ratios of the organic ligands. The FT-IR spectra, as shown in Fig. 5a, verified the presence of characteristic FT-IR peaks associated with the organic ligands across all hybrid materials. The peaks at 664, 690, and 1221 cm^{-1} were assigned to pyrimidine. Upon the substitution of pyrimidine with different amounts of pyrazine, new FT-IR peaks emerged at 486, 1058, 1148, and 1170 cm^{-1}, which correspond to distinctive vibrations of pyrazine, thereby confirming the successful integration of the pyrazine ligand within the hybrid materials (Fig. 5a–c). The variation in the peak intensities in the FT-IR spectra, which depend on the ratio of ligand replacement, further shows the gradual substitution of pyrimidine by pyrazine ligands from the NiClOH–Pm to the NiClOH–Pz stoichiometry. Further quantitative analyses by ^1H NMR spectroscopy confirmed the different ligand ratios in the hybrid materials after ligand substitution. As shown in Fig. S6, the peaks around 7.8, 8.9 and 9.2 ppm are assigned to H atoms of pyrimidine, and another peak at 8.8 ppm to the H atoms of pyrazine. The ratio of the two ligands was calculated by integrating the peak areas of the two groups of peaks, as shown in Fig. S7.

Raman spectroscopy was used to examine the structural differences between the NiClOH–Pm_xPz_{1-x} hybrid materials (Fig. 5d–f). The peaks at around 600 to 750 cm^{-1} were assigned to pyrimidine and pyrazine ligands.[47,48] When NiClOH–Pm_x-Pz_{1-x} hybrid materials are pillared by different diazine ligands (pyrimidine and pyrazine), a clear red shift of the low-frequency Raman band is observed from 142 cm^{-1} to 138 cm^{-1} upon ligand substitution (Fig. 5e and f). This band lies in the low-frequency region and is assigned primarily to the Ni–N stretching vibration, with a coupled N–Ni–N bending component. This mode involves the Ni–N bond stretching (the Ni atom moving relative to the coordinated nitrogen) and a bending of the N–Ni–N linkages in the octahedral coordination environment. The red shift of 4 cm^{-1} indicates that ligand-substitution results in a slightly higher electron density around the Ni atoms. However, within the 1020–1050 cm^{-1} spectral range, the Raman peak at 1034 cm^{-1} did not exhibit any detectable shift upon ligand replacement (Fig. 5f). This indicates that the change in electron density occurs primarily around the nickel center. This increase is attributed to the introduction of pyrazine during ligand exchange, which enhances the local electron density and alters the electronic environment of the nickel site.[49]

Inorganic–organic hybrids for electrochemical urea oxidation

The electrochemical performance of NiClOH–Pm_xPz_{1-x} hybrid materials was evaluated in 1.0 M KOH solution containing 0.5 M urea. The electrocatalytic performance of the different ligand substituted hybrid materials was systematically explored

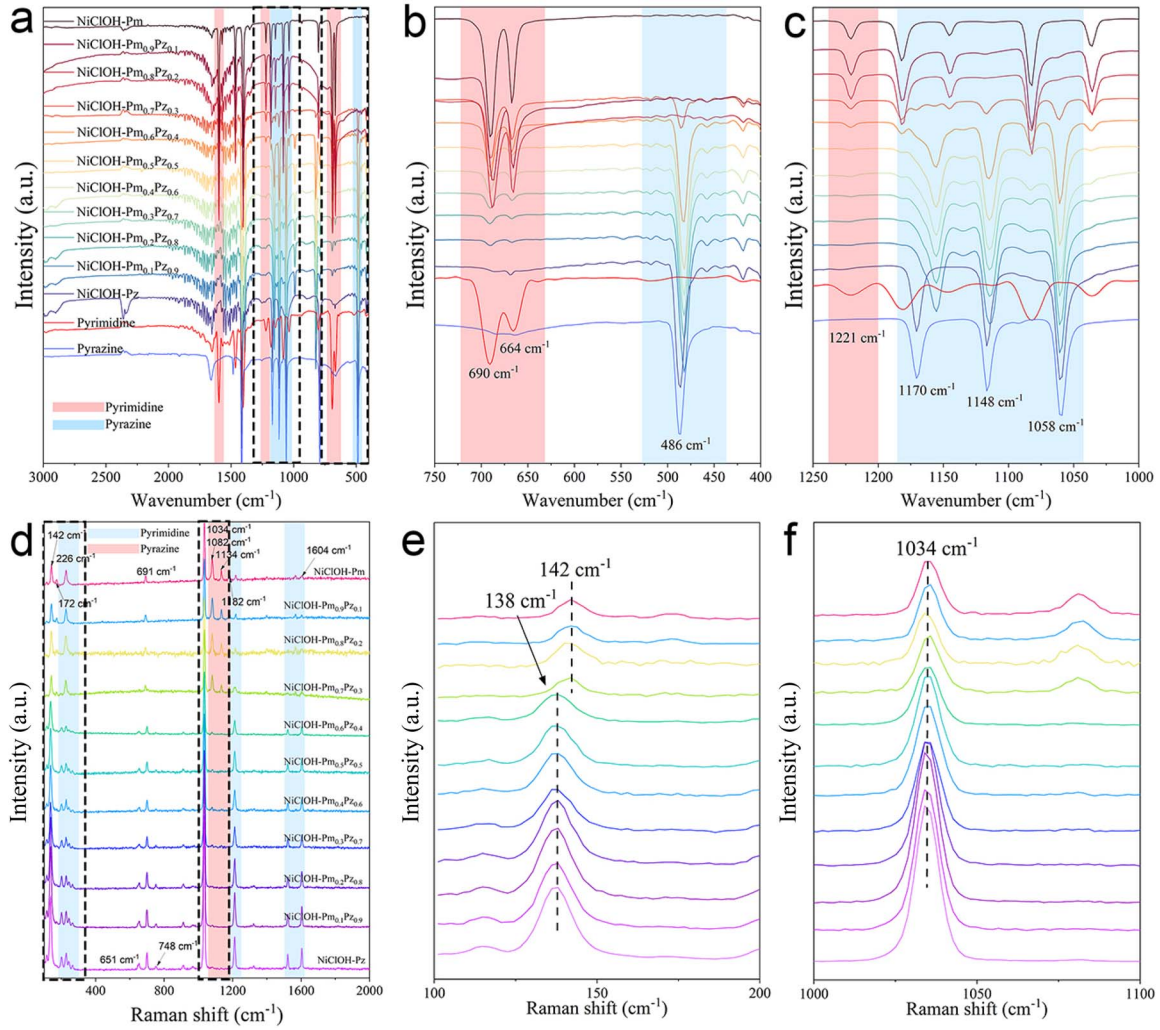

Fig. 5 (a) FT-IR spectra of NiClOH–Pm with different ratios of ligand exchange; (b and c) zoom of the highlighted area of the FT-IR spectra in panel (a); (d) Raman spectra of NiClOH–Pm, NiClOH–Pz, and different ratios of NiClOH–Pm_xPz_{1-x}; (e and f) zoom of the highlighted area of the Raman spectra in panel (b).

for the UOR (Fig. S8). The lowest potential necessary to achieve a current density of 100 mA cm^{-2} was found to be 1.53 V (*vs.* RHE) for NiClOH–$Pm_{0.8}Pz_{0.2}$, showing a notable reduction compared to the potentials observed for NiClOH–Pm and NiClOH–Pz catalysts (1.64 V and 1.89 V, respectively). This performance improvement extends to other ligand substituted hybrid materials with different ratios as shown in Fig. 6a–c and S8. The new NiClOH–$Pm_{0.8}Pz_{0.2}$ hybrid exhibits superior UOR performance compared with a broad range (oxides, hydroxides, phosphides, sulfides, and mixed-metal oxides) of reported Ni-based catalysts (Table S5).

Tafel plots obtained from LSV curves were used to evaluate the electrochemical kinetics of the hybrid materials. As shown in Fig. 6b, for UOR, NiClOH–$Pm_{0.8}Pz_{0.2}$ exhibits a Tafel slope of 41.9 mV dec^{-1}, which is smaller than those of 61.9 mV dec^{-1} for NiClOH–Pm and 64.3 mV dec^{-1} for NiClOH–Pz, respectively. The Tafel slopes of hybrid materials with other Pm/Pz ratios are all smaller than those of NiClOH–Pz and NiClOH–Pm (Fig. S9). These Tafel plots imply favorable electrocatalytic kinetics for the UOR, which is essential to understand the superior activity of NiClOH–$Pm_{0.8}Pz_{0.2}$ (Fig. 6b). Besides, OER as a reference electrochemical reaction was performed without urea for NiClOH–$Pm_{0.8}Pz_{0.2}$, which displayed a Tafel slope of 201 mV dec^{-1}, indicating that the UOR is a much better anodic reaction than OER with a lower potential and enhanced kinetics (Fig. S10).

The electrochemical double layer capacitances (C_{dl}) of NiClOH–$Pm_{0.8}Pz_{0.2}$ and other hybrids were measured using cyclic voltammetry at different scan rates and compared with those of reference samples (Fig. S11a, c and e). The current response solely results from the charging of the double layer, as indicated by CVs in the region from 0.0–0.1 V (*vs.* RHE). The C_{dl} value for NiClOH–$Pm_{0.8}Pz_{0.2}$ was calculated as 23.8 mF cm^{-2} (Fig. S11b), which is larger than those of NiClOH–Pm (14.4 mF cm^{-2}, Fig. S13d), and NiClOH–Pz (5.09 mF cm^{-2}, Fig. S11f). The C_{dl} of $Ni(OH)_2$ as a reference (Fig. S12), afforded a value of 0.718 mF cm^{-2}, which is much lower than that of all hybrid materials. The C_{dl} values correlated with the electrocatalytic surface area,

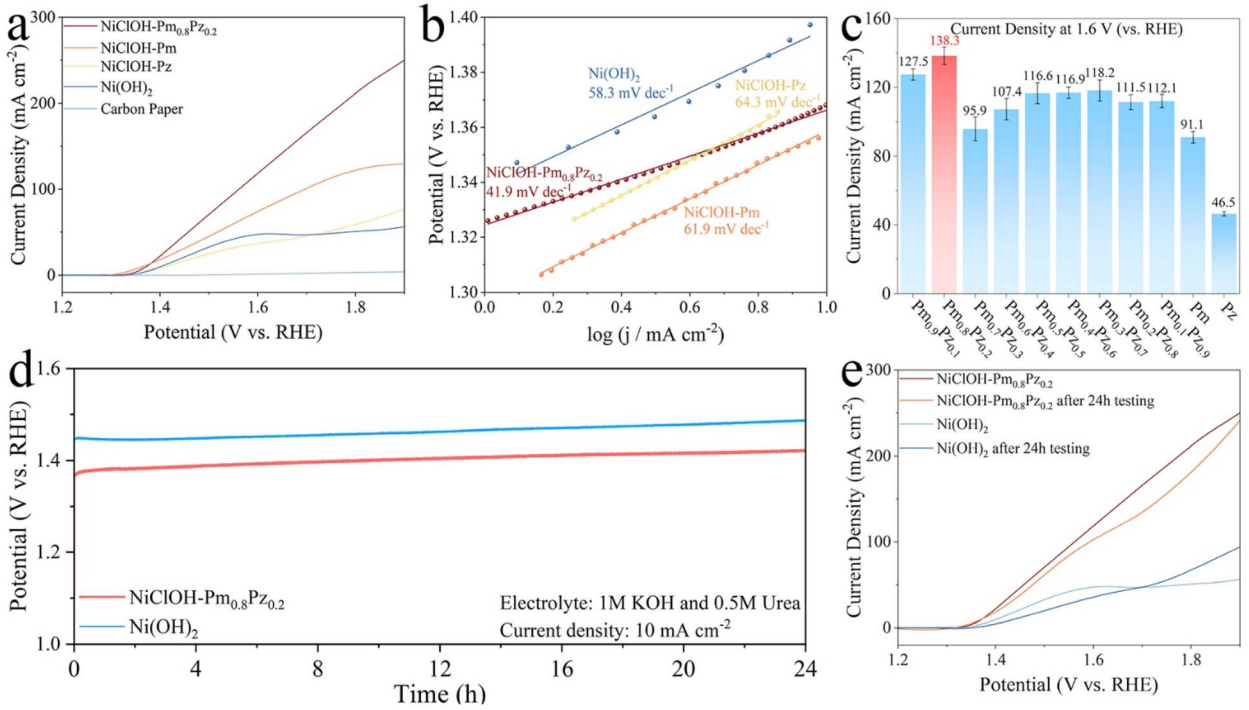

Fig. 6 (a) Polarization curves for UOR of NiClOH–$Pm_{0.8}Pz_{0.2}$ compared to $Ni(OH)_2$, NiClOH–Pm and NiClOH–Pz; (b) Tafel plots of NiClOH–$Pm_{0.8}Pz_{0.2}$, NiClOH–Pm, NiClOH–Pz and $Ni(OH)_2$; (c) comparison of the current density for the hybrid materials at 1.6 V (*vs.* RHE) for UOR; (d) chronoamperometric measurement curve at a static potential corresponding to a current density of 10 mA cm^{-2} for UOR; (e) comparison of the polarization curves before and after chronoamperometric measurement.

indicating that NiClOH–$Pm_{0.8}Pz_{0.2}$ has a larger ECSA than NiClOH–Pm and NiClOH–Pz.[50]

In addition to the analysis of Tafel slopes, we further demonstrated the superior reaction kinetics of the NiClOH–$Pm_{0.8}Pz_{0.2}$ hybrid material through other electrochemical tests. Fig. S13 displays the LSV results for the NiClOH–$Pm_{0.8}Pz_{0.2}$ catalyst in 1 M KOH electrolyte, obtained for various urea concentrations at a scan rate of 10 mV s^{-1}. For NiClOH–$Pm_{0.8}Pz_{0.2}$, the anodic peak current density, attributed to UOR performance, increases with the urea concentration (from 0.01 to 0.50 M), which can be attributed to an enhanced surface coverage of urea molecules on NiClOH–$Pm_{0.8}Pz_{0.2}$ under more concentrated conditions. This behavior indicates that UOR is predominantly a diffusion-limited process when the urea concentration is below 0.50 M. At low urea concentrations ($\leq$0.30 M), the limited surface coverage of urea restricts the current density. Increasing the urea concentration from this lower range first enhances the surface coverage, thereby boosting the anodic current density and contributing to the high intrinsic activity of NiClOH–$Pm_{0.8}Pz_{0.2}$.[51] However, when the urea concentration was adjusted to 0.50 M, the increase in current density slows down, as the UOR efficiency is limited by the occupation of active Ni sites under high urea concentrations ($\geq$0.40 M). To investigate the presence of O (or other) vacancies as possible adsorption sites, we added different potassium salts [K_2S and CH_3COOK] to the electrolyte during the UOR with NiClOH–$Pm_{0.8}Pz_{0.2}$. As shown in Fig. S14a, after adding the sulfides, the electrocatalytic performance showed a noticeable decline, confirming that some vacancy sites on the surface of hybrid NiClOH–$Pm_{0.8}Pz_{0.2}$ were occupied by the sulfides, thereby hindering subsequent reactions.[34] The same test was also performed on NiClOH–Pm (Fig. S14b), leading to a related reduction of the UOR performance in the presence of K_2S and CH_3COOK, respectively. However, the corresponding decrease in current density is significantly less than that observed for NiClOH–$Pm_{0.8}Pz_{0.2}$ in the same solution environment, which can be attributed to fewer vacancies on the surface of NiClOH–Pm. To further support the results of the poisoning tests, the EPR spectrum of NiClOH–$Pm_{0.8}Pz_{0.2}$ was recorded. As shown in Fig. S15, NiClOH–$Pm_{0.8}Pz_{0.2}$ exhibits a pronounced EPR signal at $g = 2.002$, suggesting the presence of vacancy-related paramagnetic species. The oxygen vacancies in NiClOH–$Pm_{0.8}Pz_{0.2}$ primarily originate from ligand-induced local coordination perturbations and electrochemical reconstruction under alkaline anodic polarization (*e.g.*, Cl^- leaching and the formation of vacancy-rich Ni–O species). The resulting anion/vacancy-rich Ni-(oxy)hydroxide surface provides coordinatively unsaturated active sites, thereby enhancing urea adsorption and accelerating the urea oxidation kinetics.[52] Under the same measurement conditions, no EPR signal was observed for $Ni(OH)_2$, which is attributed to its fully hydroxylated structure, lack of unstable anions, and unfavourable vacancy-related electron trapping stability.[53] For UOR, at a static current density of 10 mA cm^{-2} (Fig. 6d) NiClOH–$Pm_{0.8}Pz_{0.2}$ remained stable over 24 h without much performance reduction. After comparing the LSV curves before and after testing, the potential only increased by 0.21 V (Fig. 6e) at a current density of 100 mA cm^{-2}. Also, NiClOH–$Pm_{0.8}Pz_{0.2}$ was stable in multi-current tests from 10 to

110 mA cm^{-2} (Fig. S16). In contrast, $Ni(OH)_2$ does not withstand current densities above 60 mA cm^{-2} (Fig. S16). To further test the long-term performance of NiClOH–$Pm_{0.8}Pz_{0.2}$, a chronoamperometry (CA) test was conducted on NiClOH–$Pm_{0.8}Pz_{0.2}$ at 1.53 V for 100 h (Fig. S16b). The results showed that after 100 h of UOR, the current loss was less than 5%, indicating that although NiClOH–$Pm_{0.8}Pz_{0.2}$ leached chloride ions during the process, the overall performance did not change significantly. The selectivity, Faradaic efficiency and H_2 evolution rate were measured *via* gas chromatography (GC), as shown in Fig. S17. The selectivity of UOR on the anode is around 98% (when the selectivity is greater than 98%, the O_2 evolution rate is below the GC detection limit). On the cathode, the average H_2 evolution rate is around 1.11 μL s^{-1} and the corresponding Faradaic efficiency is around 97.4%. By analyzing and calculating the urea amount in the electrolyte before and after the reaction using ^{13}C NMR spectroscopy, the overall Faradaic efficiency for the UOR for 24 h was found to be about 95.1% (Fig. S18). Therefore, we used commercial solar panels as the energy source for practical electrolysis, and the electrocatalyst works smoothly when driven by solar power in 1.0 M KOH and 0.5 M urea electrolyte (SI Video).

Beyond UOR, the hybrid electrocatalyst exhibits exceptional efficiency in alcohol-based biomass oxidation reactions, as illustrated in Fig. S19. In various biomass solutions such as methanol, ethanol, and glycerin, even though NiClOH–$Pm_{0.8}Pz_{0.2}$ is not always the best electrocatalyst among the substitutional series for all the reactions, this specific hybrid materials consistently exhibited lower potentials at a current density of 10 mA cm^{-2} compared to $Ni(OH)_2$ and various other representative electrocatalysts (Fig. S20 and Table S6). NiClOH–$Pm_{0.8}Pz_{0.2}$ was also tested for long-term stability in 1.0 M KOH and 0.50 M in different biomass solutions (urea, methanol, ethanol, benzyl alcohol, and glycerin). As for other alcohol-based biomass substrates (methanol, ethanol, benzyl alcohol, and glycerin, Fig. S21), NiClOH–$Pm_{0.8}Pz_{0.2}$ also shows better performance and stability than $Ni(OH)_2$ (Fig. S22).

In situ Raman spectroscopy (Fig. 7d) was used to monitor the urea adsorption and to check for intermediates of NiClOH–$Pm_{0.8}Pz_{0.2}$ during electrocatalysis. In previous works,[21] NiOOH was reported to be the active intermediate for UOR. Once NiOOH was excessively accumulated, however, it undergoes further oxidation to form another active intermediate, $Ni^{2+\delta}O_xH_y$, which favors the competing OER over the UOR.[17] Peaks assigned to urea (731, 1007, and 1064 cm^{-1}) were appearing over time (Fig. 7d), indicating that urea adsorption proceeds from 1.0 V onwards. A pair of peaks typical of $Ni^{2+\delta}O_xH_y$ were reported to appear at 400–600 cm^{-1} in the *in situ* Raman spectra of $Ni^{2+\delta}O_xH_y$.[23,37] Importantly, such peaks were not found for NiClOH–$Pm_{0.8}Pz_{0.2}$ in 1 M KOH and 0.5 M urea (Fig. 7d). This indicates that the dominant inorganic active intermediate at the Ni sites is NiOOH rather than $Ni^{2+\delta}O_xH_y$. It further implies that the catalyst facilitates a fast transfer of hydrogen from urea molecules, preventing a substantial accumulation of NiOOH, thus improving the UOR performance. As NiOOH drives the oxidation of N-containing species, it is more effective than $Ni^{2+\delta}O_xH_y$ in facilitating the dehydrogenation and bond-cleavage rearrangements of urea, thus giving rise to the high activity and selectivity of NiClOH–$Pm_{0.8}Pz_{0.2}$.[23] At a potential of 1.0 V, the *in situ* Raman spectrum shows several peaks between 1000–1050 cm^{-1}, corresponding to urea adsorbed on the electrocatalyst surface. The peak at 731 cm^{-1} assigned to the C–N bond displayed slightly increasing intensity with the measurement time due to the enhanced urea adsorption and the π–π interaction of ligands during the electrocatalytic measurements, which enhanced the electron transfer during UOR. When the potential was removed, all peaks disappeared except for a single one at 1033 cm^{-1} indicating the adsorption of urea on the surface of the electrocatalysts. From DFT calculations (*cf.* below and Fig. 7a), it is furthermore evident that NiClOH–$Pm_{0.8}Pz_{0.2}$ displays a stronger tendency to adsorb urea rather than OH^-.

Post-catalytic characterizations

After 24 h of chronoamperometric measurements, the PXRD pattern (Fig. S23) of post-catalytic NiClOH–$Pm_{0.8}Pz_{0.2}$ showed $Ni(OH)_2$ as the main phase (JCPDS no. 14-0117), and some weak peaks at 15.4 and 20.3° attributed to NiOOH (JCPDS no. 27-0956). The post-catalytic XANES Ni K-edge spectrum of NiClOH–$Pm_{0.8}Pz_{0.2}$ (Fig. S24a) was shifted to slightly higher energy than $Ni(OH)_2$ (Fig. S24a). The EXAFS spectra of post-catalytic NiClOH–Pm and NiClOH–$Pm_{0.8}Pz_{0.2}$ show two main peaks at 1.62 and 2.82 Å arising from backscattering from first and second shell coordinated O and Ni atoms at interatomic distances of Ni–O = 2.06 Å and Ni–Ni = 3.11 Å for both post-catalytic NiClOH–Pm and NiClOH–$Pm_{0.8}Pz_{0.2}$ (Fig. S24 and Table S1). These structural features in the EXAFS spectra of post-catalytic NiClOH–Pm and NiClOH–$Pm_{0.8}Pz_{0.2}$ resemble those in the EXAFS spectrum of reference $Ni(OH)_2$, indicating the transformation of NiClOH–Pm and NiClOH–$Pm_{0.8}Pz_{0.2}$ into a $Ni(OH)_2$-related phase during UOR. SEM and EDX analyses were conducted to assess the morphological changes during the electrocatalysis process. As illustrated in Fig. S25 and S26, the morphology of the nanorods remained partially unchanged, exhibiting a slight extent of agglomeration. EDX mapping (Fig. S27) revealed that these nanorods maintained a uniform elemental distribution similar to that before the reaction. EDX spot analyses indicated that the average Ni content was not much changed before and after the UOR (Table S2 and S3). However, the average Cl content decreased significantly compared with pristine NiClOH–$Pm_{0.8}Pz_{0.2}$, corresponding with the transformation of the NiClOH inorganic component to a $Ni(OH)_2$-related phase. This is in line with ICP-MS results (Table S4), which show lower post-catalytic Cl/Ni ratios, albeit less drastic Cl losses than on the sample surface. Furthermore, Raman spectroscopy was also employed to assess the changes of the materials after UOR. As shown in Fig. S28, even for a lower intensity and higher signal-to-noise ratio of the measured Raman spectra, both the post-catalytic materials and $Ni(OH)_2$ exhibited a similar, very broad Raman peak assigned to –OH groups around 1370 cm^{-1}, further confirming that the inorganic component of the hybrid materials transformed into $Ni(OH)_2$-related species during the electrocatalytic process.

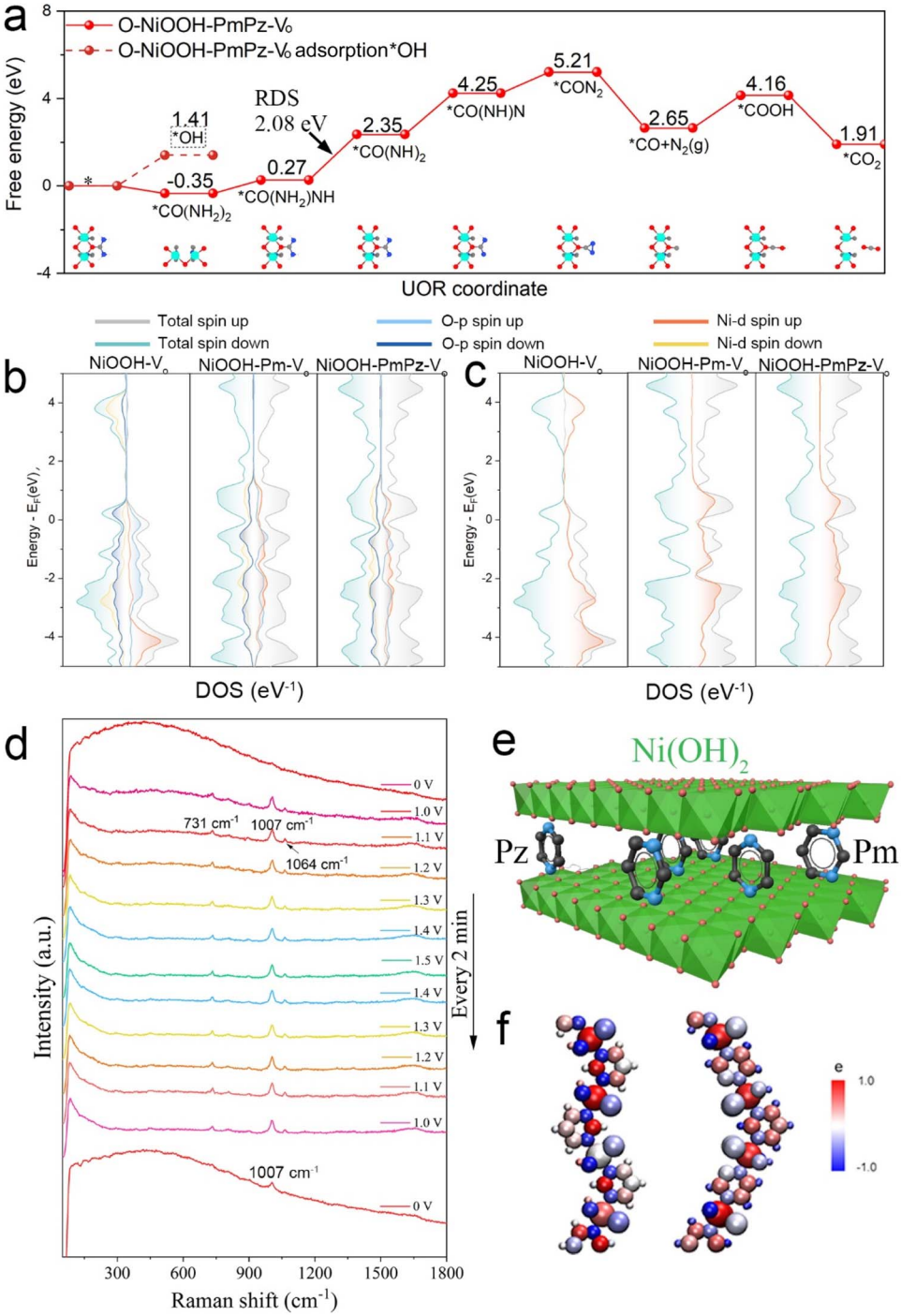

Fig. 7 (a) Free energy diagram for UOR in NiClOH–PmPz-V_O (* represents the substrate); (b) contribution of Ni and O to the electronic density on the surface layer; (c) contribution of the different Ni $3d_{z^2}$ orbitals to the DOS of the NiOOH single layer, NiOOH–Pm and NiOOH–PmPz with V_O (from left to right); the d band centers of all the post catalysts are given in the panel; (d) *in situ* Raman spectra during UOR in 1 M KOH and 0.5 M urea from 0 to 1.5 V (*vs.* RHE); (e) schematic illustration of the $Ni(OH)_2$–PmPz related hybrid motif after UOR (the rings represent Pm and Pz ligands as schematic placeholders rather than an SC-XRD-derived model); (f) DFT calculation of the electron density of NiClOH–Pm (left) and NiClOH–$Pm_{0.8}Pz_{0.2}$ (right).

Besides, several peaks remaining between 100–300 cm^{-1} can be assigned to organic ligands. FT-IR spectra (Fig. S29) showed similar results: at ~500 cm^{-1}, the post-catalyst displayed a related absorption peak as for $Ni(OH)_2$, as well as double peaks at ~1350, and ~1650 cm^{-2} assigned to –OH vibrations. XP spectra were furthermore recorded for NiClOH–$Pm_{0.8}Pz_{0.2}$ after 24 h long term UOR tests (Fig. S30). The Ni XP spectrum shows Ni^{2+} and Ni^{3+} peaks attributed to the post-catalytic phase and to some extent of surface oxidation. The N 1s XP spectrum shows a peak at 400.5 eV, which is a typical signal of N atoms

located in aromatic rings, indicating the presence of Pm and Pz ligands. Additionally, the electrolyte was carefully checked with ^{1}H NMR spectroscopy (Fig. S31), and no peaks of organic ligands were found after 24 h of testing. NiClOH–$Pm_{0.8}Pz_{0.2}$ after 24 h of electrocatalytic testing of other biomass oxidation reactions was also checked with Raman spectroscopy (Fig. S32) and SEM (Fig. S33), showing similar results as post-catalytic $Ni(OH)_2$–PmPz after UOR. Post-catalytic XP (Fig. S30) and Raman spectra (Fig. S32) confirm the retention of Pm/Pz ligands, as evidenced by the Ni–N vibration (252 cm^{-1}) and the N 1s peak at ~400.5 eV. The broadened (110) (Fig. S23) reflection in the post-catalytic PXRD further supports ligand intercalation between $Ni(OH)_2$ layers. Together with literature and DFT reports,[34] these results indicate that the post-catalytic phase corresponds to a layered $Ni(OH)_2$ structure with intercalated ligands. With these data at hand, the post-electrocatalyst can best be described as a Pm- or Pz-supported layered $Ni(OH)_2$-type hybrid, closely resembling the pillar-coordinated $Ni(OH)_2$ structures reported in the literature (schematic representation in Fig. 7e).[54,55] Accordingly, the subsequent DFT calculations for the active species were performed using a NiOOH–PmPz model with oxygen vacancies to reflect the *in situ* Raman results and the observed structural transformations of the hybrid material after surface Cl-leaching.

DFT calculations and proposed catalytic mechanism

DFT calculations were performed on three slabs of reference octahedral NiOOH (oct-NiOOH) monolayer, NiOOH–Pm, and NiOOH–PmPz to explore the observed trends in the UOR activity. Following the nomenclature adopted here, the hybrid pillared structures are denoted as NiOOH–Pm and NiOOH–PmPz, while the models for the surface vacancy-containing derivatives formed after Cl leaching are labelled NiOOH–Pm-V_O and NiOOH–PmPz-V_O. The adsorption energies of urea on the NiOOH surface, compared with *OH, provide critical insights into its catalytic efficiency for UOR. The competitive adsorption of $*CO(NH_2)_2$ and *OH on NiOOH was examined in previous studies.[20,34] As shown in Fig. 7a, the adsorption energy of $*CO(NH_2)_2$ on NiOOH–PmPz-V_O is −0.35 eV, which is significantly lower than the absorption energy of *OH (1.41 eV, Fig. 7a). This indicates that the urea molecule is more easily adsorbed on the active Ni sites compared to *OH, enhancing the UOR selectivity, in line with the electrochemical test results (Fig. S16). The energy level calculations for UOR revealed distinct rate-determining steps for each model. For NiOOH–PmPz, the rate-determining step is the dehydrogenation process involving the cleavage of the N–H bond in urea, while for NiOOH–Pm, it is urea adsorption (Fig. S34 and S35). Urea can adsorb onto the catalyst surface in two ways: *via* the O atom or the N atom at the Ni site. These adsorption modes alter the H–N–H configuration of urea, affecting the ease of N–H bond cleavage. Oxygen vacancies further enhance the adsorption selectivity, resulting in more favourable O adsorption on the Ni sites of NiOOH–PmPz-V_O (Fig. S35). This selectivity also impacts the deprotonation process on the NiOOH–PmPz catalyst surface.[50] Without vacancies, the overall free energy change for the four-step N–H cleavage to $*CON_2$ is favourable at −0.22 eV, with the N–Ni adsorption configuration being preferred. However, with vacancies, O–Ni adsorption is favoured, and the overall deprotonation process becomes challenging, with the transition from –NH_2 to –NH requiring an energy barrier of −2.08 eV, rendering it the rate-determining step of the UOR (Fig. 7a and S35). Overall, the DFT calculation results suggest that the Ni centers in both NiOOH–Pm and NiOOH–PmPz retain an [Ni–O_4–N_2] octahedral coordination. NiOOH–PmPz-V_O combines strong, selective urea chemisorption with the lowest kinetic barrier for N–H cleavage, fully accounting for the enhanced alkaline UOR performance observed after structural reconstruction of NiClOH–PmPz. While this mechanistic model is coherent, the possibility of a lattice oxygen mechanism needs to be excluded in future studies on ^{18}O labelled NiClOH–$Pm_{0.8}Pz_{0.2}$.

To elucidate the UOR mechanism on the NiOOH–PmPz surface, we conducted a detailed analysis of the three models and examined the electronic structure of the Ni-d orbitals (Fig. 7b). The overall DOS reveals that all three systems (NiOOH–V, NiOOH–Pm-V_O, and NiOOH–PmPz-V_O) exhibit significant spin asymmetry, indicating the presence of a net magnetic moment,[40,43] consistent with the partially filled d orbitals of Ni in NiOOH. In the O-p projected DOS (Fig. 7b), the −2 to −4 eV energy region is dominated by the O-2p band, while NiOOH–PmPz-V_O exhibits a higher O-p density of states near the Fermi level (E_F), indicating stronger electronic coupling between O and Ni, and that O atoms are more readily involved in charge transfer processes. The Ni-d projected DOS (Fig. 7c) further reveals the differences in the local electronic environment of the metal center in the three structures. Compared with NiOOH–V, both NiOOH–Pm-V_O and NiOOH–PmPz-V_O show a substantially higher Ni-d state density near the Fermi level. Such an increased Ni-d contribution in the vicinity of the Fermi level indicates improved electronic conductivity. This characteristic indicates that the Pm and Pz ligands can effectively modulate the electronic structure of Ni sites, enabling the establishment of more accessible empty d orbitals, which is beneficial for faster the electron transfer during catalysis. The Pm and Pz ligands and oxygen vacancies together endow NiOOH–PmPz-V_O with higher O-p and Ni-d state densities, stronger spin polarization, and more pronounced defect state distribution, providing the ligand-substituted catalyst with superior electronic transport properties and thereby faster electron transfer. These factors all contribute to its higher activity in electrocatalytic reactions.

Further analysis of the electronic distribution in different Ni-d orbital directions revealed that the d_{z^2} orbital in the NiOOH single layer exhibited spin polarization (Fig. 7c). However, the d_{z^2} orbitals of NiOOH–OH–PmPz-V_O (Fig. S37) showed a significant difference of spin-up and spin-down near E_F, indicating that NiOOH–PmPz-V_O promotes electron migration to the surface, thereby reducing the reaction barrier. When comparing NiOOH–OH–PmPz-V_O with the other structures without vacancies (NiOOH-SL, NiOOH–Pm, and NiOOH–PmPz, Fig. S36, S38 and S40), the NiOOH–PmPz material containing V_O exhibits a significantly enhanced DOS near the Fermi level (Fig. S41),

indicating that vacancy-induced materials effectively improve the electronic conductivity. In addition, considering that the active intermediate of $Ni(OH)_2$ is usually a single layer (SL) of NiOOH, the DOS of NiOOH-SL and NiOOH-SL-V_O were also calculated for comparison. When compared to NiOOH-SL and NiOOH-SL-V_O (Fig. S38 and S39), which lack Pm and Pz ligands, the orbital-resolved DOS of NiOOH–PmPz-V_O shows a significant low-energy shift of all Ni 3d orbital levels (Fig. S39). This should be attributed to the strengthened Ni–N electronic coupling, which stabilizes the t_{2g} orbitals and makes the e_g orbitals more accessible. Upon comparing two materials with similar organic ligands and vacancies (NiOOH–Pm-V_O and NiOOH–PmPz-V_O), there were no apparent differences between NiOOH–Pm-V_O and NiOOH–PmPz-V_O. Only at E_F and energies below, NiOOH–PmPz-V_O exhibits stronger conductivity and a lower energy of the t_{2g} orbitals (Fig. 7f, S41 and S43). This demonstrates that the introduction of mixed ligands has a positive impact on the catalytic activity of the material. As a result, NiOOH–PmPz-V_O exhibits more favourable electronic properties for accelerating urea activation and oxidation.

Conclusions

In this study, we introduce a ligand substitution strategy that incorporates pyrimidine (Pm) and pyrazine (Pz) ligands into a Ni-based organic–inorganic hybrid material. The optimized mixed–ligand hybrid catalyst, NiClOH–$Pm_{0.8}Pz_{0.2}$, exhibits excellent UOR performance, requiring only 1.37 and 1.53 V (*vs.* RHE) to deliver current densities of 10 and 100 mA cm^{-2}, respectively, together with a low Tafel slope (41.9 mV dec^{-1}) and a high electrochemical double-layer capacitance. Post-catalytic XAS and *in situ* Raman spectroscopy both indicate that the material undergoes electrochemical reconstruction into a ligand-supported NiOOH species, which serves as the true active phase during UOR and furthermore shows promising performance in several biomass-derived electrolytes. NiClOH–$Pm_{0.8}Pz_{0.2}$ excels through facilitated reconstruction into an active NiOOH inorganic component supported by Pm and Pz ligands during UOR. Rather than converting into simple $Ni(OH)_2$, the post-catalytic phase preserves a hybrid Ni–O/N coordination environment, along with surface oxygen vacancies (V_O), which is reflected in the structural motifs for our DFT models. DFT calculations further demonstrate that mixed ligand engineering of pyrimidine and pyrazine increases the Ni-d/O-p density of states near E_F to alter the local electronic structure of NiOOH. The improved electronic structure of NiOOH–PmPz-V_O accounts for the enhanced UOR kinetics. Overall, this work establishes ligand substitution as a viable strategy for tailoring the coordination and electronic structure of Ni-based hybrid precursors, enabling highly active and robust NiOOH-related hybrid phases for urea-assisted water splitting and other biomass oxidation reactions.

Author contributions

Lingshen Meng conceived the idea, designed the research project, performed the experiments, collected and analysed the data and co-wrote the manuscript. Zeyi Zhang performed the computational DFT calculations and co-wrote the manuscript. Carlos A. Triana designed the research project, collected and analysed the XAS data and contributed to reviewing the paper. Aaron A. Schultz collected and analysed the GC data. Hang Chen and Dan Zhang contributed to the sample characterizations. Greta R. Patzke conceived the idea, designed the research project, edited and reviewed the paper, and provided support for the project. All authors discussed the results and commented on the paper.

Conflicts of interest

The authors declare no conflict of interest.

Data availability

The data supporting this article have been included as part of the supporting information (SI). Supplementary information: Fig. S1–S43, Table S1–S6 and SI Video. See DOI: https://doi.org/10.1039/d5ta10043g.

Acknowledgements

This work was supported by the University of Zurich Research Priority Program *Solar Light to Chemical Energy Conversion* (URPP LightChEC). Zeyi Zhang, Dan Zhang, and Hang Chen thank the China Scholarship Council (CSC) for supporting their PhD fellowships. We are grateful to Dr Dragos Stoian and Dr Wouter van Beek at the Swiss-Norwegian beamline SNBL-BM31 at ESRF for allocation of synchrotron radiation and to Dr René Verel (ETH Zurich) for his assistance with the NMR measurements. We are also grateful for Jiaxin Wang (Jilin University) for help with XP spectra.

References

1 A. Yu, Y. Zhang, S. Zhu, T. Wu and Z. J. Xu, Spin-related and non-spin-related effects of magnetic fields on water oxidation, *Nat. Energy*, 2025, **10**(4), 435.
2 H. Zhao, F. Tian, W. Xiao, G. Xu, X. Zhang, L. Wang and Z. Wu, Microwave-synthesized PtFe alloy nanosheets on nickel foam for efficient overall water splitting via synergistic HER/OER optimization mechanism, *Chem. Eng. J.*, 2025, **522**, 167641.
3 X. Fu, H. Li, Y. Zong, W. Xiao, J. Wang, H. Li, T. Ma, Z. Wu and L. Wang, Ultrafast construct local acidic microenvironment of boron-intercalated osmium with anti-precipitation and corrosion-resistant for seawater-splitting, *Angew. Chem., Int. Ed.*, 2025, **64**(40), e202512710.
4 X. Fu, X. Zang, J. Gao, H. Li, W. Xiao, Y. Zong, G. Fu, J. Wang, T. Ma, W. Jin, *et al.*, Ultrafast microwave quasi-solid-state construction of Os-OsP_2 with enhanced interfacial spillover for seawater-based anion exchange membrane electrolyzers, *Adv. Energy Mater.*, 2025, **15**(30), 2501054.
5 S. Xu, X. Ruan, M. Ganesan, J. Wu, S. K. Ravi and X. Cui, Transition metal-based catalysts for urea oxidation reaction (UOR): catalyst design strategies, applications, and future perspectives, *Adv. Funct. Mater.*, 2024, **34**(18), 2313309.

6 X. Gao, X. Bai, P. Wang, Y. Jiao, K. Davey, Y. Zheng and S.-Z. Qiao, Boosting urea electrooxidation on oxyanion-engineered nickel sites via inhibited water oxidation, *Nat. Commun.*, 2023, **14**(1), 5842.

7 N. N. Rao, C. Alex, M. Mukherjee, S. Roy, A. Tayal, A. Datta and N. S. John, Evidence for exclusive direct mechanism of urea electro-oxidation driven by *in situ*-generated resilient active species on a rare-earth nickelate, *ACS Catal.*, 2024, **14**(2), 981.

8 G. Kalaiyarasan, D. Lee, J. W. Lee and M. J. Ko, Electrochemical synthesis of nickel hexacyanoferrate and nickel sulfide on nickel foam as sustainable electrocatalysts for hydrogen generation via urea electrolysis, *ACS Appl. Mater. Interfaces*, 2024, **16**(50), 69142.

9 X. Guo, Y. Li, Z. Xu, D. Liu, A. Kong and R. Liu, Interface electron transfer direction-tuned urea electrooxidation over multi-interface nickel sulfide heterojunctions, *Small*, 2025, **21**(4), 2408908.

10 H. Jiang, M. Sun, S. Wu, B. Huang, C.-S. Lee and W. Zhang, Oxygen-incorporated NiMoP nanotube arrays as efficient bifunctional electrocatalysts for urea-assisted energy-saving hydrogen production in alkaline electrolyte, *Adv. Funct. Mater.*, 2021, **31**(43), 2104951.

11 H. Liu, S. Zhu, Z. Cui, Z. Li, S. Wu and Y. Liang, Ni_2P nanoflakes for the high-performing urea oxidation reaction: linking active sites to a UOR mechanism, *Nanoscale*, 2021, **13**(3), 1759.

12 P. Li, W. Li, Y. Huang, Q. Huang and S. Tian, 3d hierarchical-architectured nanoarray electrode for boosted and sustained urea electro-oxidation, *Small*, 2023, **19**(30), 2300725.

13 C. Pei, S. Chen, T. Zhao, M. Li, Z. Cui, B. Sun, S. Hu, S. Lan, H. Hahn and T. Feng, Nanostructured metallic glass in a highly upgraded energy state contributing to efficient catalytic performance, *Adv. Mater.*, 2022, **34**(26), 2200850.

14 Y. Zhang, X. Zhen, Z. Su, J. Guo, J. Li, L. shuai and X. Li, Ni/MoC@NC as bifunctional electrocatalyst coupled HER and urea oxidation for energy-efficient hydrogen production, *Int. J. Hydrogen Energy*, 2024, **60**, 46.

15 Y. Feng, N. Ran, X. Wang, Q. Liu, J. Wang, L. Liu, K. Suenaga, W. Zhong, R. Ma and J. Liu, Nanoparticulate WN/Ni_3C coupling in ceramic coatings for boosted urea electro-oxidation, *Adv. Energy Mater.*, 2023, **13**(42), 2302452.

16 N. Sinha and P. Roy, Nickel–vanadium–manganese trimetallic nitride as energy saving, efficient bifunctional electrocatalyst for alkaline water splitting via urea electrocatalysis, *Inorg. Chem.*, 2023, **62**(8), 3349.

17 H. Zhao, S. Liu, F. Tian, H. Li, L. Xin, W. Xiao, G. Xu, D. Chen, T. Ma, E. Egamberdiev, *et al.*, Trace cobalt accelerates the structural reconstruction to generate high-valence nickel for water-splitting in seawater media, *Chem. Eng. J.*, 2025, **515**, 163388.

18 M. Liu, W. Zou, S. Qiu, N. Su, J. Cong and L. Hou, Active site tailoring of Ni-based coordination polymers for high-efficiency dual-functional HER and UOR catalysis, *Adv. Funct. Mater.*, 2024, **34**(3), 2310155.

19 J. Gautam, S.-Y. Lee and S.-J. Park, Cutting-edge optimization strategies and in situ characterization techniques for urea oxidation reaction catalysts: a comprehensive review, *Adv. Energy Mater.*, 2025, (15), 2406047.

20 W. Chen, L. Xu, X. Zhu, Y. C. Huang, W. Zhou, D. Wang, Y. Zhou, S. Du, Q. Li, C. Xie, *et al.*, Unveiling the electrooxidation of urea: intramolecular coupling of the N-N bond, *Angew. Chem., Int. Ed.*, 2021, **60**(13), 7297.

21 P. Guo, S. Cao, W. Huang, X. Lu, W. Chen, Y. Zhang, Y. Wang, X. Xin, R. Zou, S. Liu and X. Li, Heterojunction-induced rapid transformation of Ni^{3+}/Ni^{2+} sites which mediates urea oxidation for energy-efficient hydrogen production, *Adv. Mater.*, 2024, **36**(18), 2311766.

22 C. Ji, H. Duan, C. Wang, G. Liang, X. Long, X. She, R. Zhang, F. Gong, D. Li, D. Yang and J. Liu, Pairing N-vacancy and adjacent Ni-sites in the local microenvironment to regulate the urea oxidation reaction pathway with enhanced kinetics, *Adv. Mater.*, 2025, 2503879.

23 Y. Tong, P. Chen, M. Zhang, T. Zhou, L. Zhang, W. Chu, C. Wu and Y. Xie, Oxygen vacancies confined in nickel molybdenum oxide porous nanosheets for promoted electrocatalytic urea oxidation, *ACS Catal.*, 2018, **8**(1), 1.

24 R. Deng, M. Guo, C. Wang and Q. Zhang, Recent advances in cobalt phosphide-based materials for electrocatalytic water splitting: from catalytic mechanism and synthesis method to optimization design, *Nano Mater. Sci.*, 2024, **6**(2), 139.

25 K. Wang, M. Pei, Y. Shuai, Y. Liu, S. Deng, Z. Zhuang, K. Sun, W. Yan and J. Zhang, Rapid two surface reconstructions of Ni/MnO heterojunction for superior urea electrolysis, *ACS Energy Lett.*, 2024, **9**(9), 4682.

26 L. Chen, W. Jiang, J. Zhang, B. Chu, Z. Zhai, T. Yu, H. He and S. Yin, Comprehensive understanding of the electrocatalytic mechanism for Co/Fe/Cu doped $Ni(OH)_2$ on urea oxidation reactions: theory and experiment, *ACS Sustain. Chem. Eng.*, 2024, **12**(28), 10466.

27 X. Fan, Z. Fu, J. Lin, B. He, J. Zhang, E. Hu and Z. Chen, Modulation of energy barrier of reaction steps over S-doped $Ni(OH)_2$/Cu composites to achieve high-performance urea electrolysis catalysts, *Chem. Eng. J.*, 2024, **490**, 151251.

28 Q. Chen, X. Deng, H. He, L. Jiang, C. Liang, J. Zhang, R. Wang and J. Chen, Modulating nanostructure and electronic structure of P and W co-doped carbon encapsulated heterovalent nico composite for accelerating urea oxidation reaction, *Chem. Eng. J.*, 2024, **484**, 149561.

29 Z. Wang, M. Zhang, X. Liu, H. Gao, C. Song and D. Wang, S-doped $Ni_{0.5}Co_{0.5}Fe_2O_4$ porous single-crystalline nanosheets for electrocatalytic oxygen evolution, *ACS Appl. Nano Mater.*, 2024, **7**(6), 6196.

30 H. Jiang, J. Xia, L. Jiao, X. Meng, P. Wang, C.-S. Lee and W. Zhang, Ni single atoms anchored on N-doped carbon nanosheets as bifunctional electrocatalysts for urea-assisted rechargeable Zn-air batteries, *Appl. Catal., B*, 2022, **310**, 121352.

31 F. Luo, S. Pan, Y. Xie, C. Li, Y. Yu and Z. Yang, Atomically dispersed Ni electrocatalyst for superior urea-assisted water splitting, *J. Energy Chem.*, 2024, **90**, 1.

32 L. Jin, R. Ji, H. Wan, J. He, P. Gu, H. Lin, Q. Xu and J. Lu, Boosting the electrocatalytic urea oxidation performance by amorphous–crystalline Ni-TPA@NiSe heterostructures and mechanism discovery, *ACS Catal.*, 2023, **13**(1), 837.

33 D. Zhang, L. Sun, C. Wang, Q. Xue, J. Feng, W. Ran and T. Yan, An open-framework structured material: $[Ni(en)_2]_3[Fe(CN)_6]_2$ as a cathode material for aqueous sodium- and potassium-ion batteries, *ACS Appl. Mater. Interfaces*, 2022, **14**(14), 16197.

34 Z. Chen, J. Li, L. Meng, J. Li, Y. Hao, T. Jiang, X. Yang, Y. Li, Z. P. Liu and M. Gong, Ligand vacancy channels in pillared inorganic-organic hybrids for electrocatalytic organic oxidation with enzyme-like activities, *Nat. Commun.*, 2023, **14**(1), 1184.

35 B. J. Burnett, P. M. Barron, C. Hu and W. Choe, Stepwise synthesis of metal–organic frameworks: replacement of structural organic linkers, *J. Am. Chem. Soc.*, 2011, **133**(26), 9984.

36 M. Liu, W. Zou, J. Cong, N. Su, S. Qiu and L. Hou, Identifying and unveiling the role of multivalent metal states for bidirectional UOR and HER over Ni, Mo-trithiocyanuric based coordination polymer, *Small*, 2023, **19**(44), 2302698.

37 M. Ajmal, X. Guo, M. A. Memon, M. Asim, C. Shi, R. Gao, L. Pan, X. Zhang, Z.-F. Huang and J.-J. Zou, Ligand-regulated Ni-based coordination compounds to promote self-reconstruction for improved oxygen evolution reaction, *J. Mater. Chem. A*, 2024, **12**(29), 18294.

38 J. Wang, Y.-C. Huang, Y. Wang, H. Deng, Y. Shi, D. Wei, M. Li, C.-L. Dong, H. Jin, S. S. Mao and S. Shen, Atomically dispersed metal–nitrogen–carbon catalysts with d-orbital electronic configuration-dependent selectivity for electrochemical CO_2-to-CO reduction, *ACS Catal.*, 2023, **13**(4), 2374.

39 C. Zhang, J. Cheng, Q. Wu, S. Hou, S. Feng, B. Jiang, C. J. Lambert, X. Gao, Y. Li and J. Li, Enhanced π-π stacking between dipole-bearing single molecules revealed by conductance measurement, *J. Am. Chem. Soc.*, 2023, **145**(3), 1617.

40 M. Cortijo, S. Herrero, R. Jiménez-Aparicio and E. Matesanz, Modulation of the magnetic properties of two-dimensional compounds $[NiX_2(N–N)]$ by tailoring their crystal structure, *Inorg. Chem.*, 2013, **52**(12), 7087.

41 G. A. Dawson, M. C. Seith, M. C. Neary and T. Diao, Redox activity and potentials of bidentate N-ligands commonly applied in nickel-catalyzed cross-coupling reactions, *Angew. Chem., Int. Ed.*, 2024, **63**(48), e202411110.

42 F. Wu, J. Tian, Y. Su, J. Wang, C. Zhang, L. Bao, T. He, J. Li and S. Chen, Effect of Ni^{2+} content on lithium/nickel disorder for Ni-rich cathode materials, *ACS Appl. Mater. Interfaces*, 2015, **7**(14), 7702.

43 D. Q. Yang, B. Hennequin and E. Sacher, XPS demonstration of π−π interaction between benzyl mercaptan and multiwalled carbon nanotubes and their use in the adhesion of Pt nanoparticles, *Chem. Mater.*, 2006, **18**(21), 5033.

44 H. Xu, S. Zhu, K. Lu, H. Jia, M. Xia and F. Wang, Preparation of hierarchically floral ZIF-8 derived carbon@polyaniline@Ni/Al layered double hydroxides composite with outstanding removal phenomenon for saccharin, *Chem. Eng. J.*, 2022, **450**, 138127.

45 F. Négrier, E. Marceau, M. Che, J.-M. Giraudon, L. Gengembre and A. Löfberg, A systematic study of the interactions between chemical partners (metal, ligands, counterions, and support) involved in the design of Al_2O_3-supported nickel catalysts from diamine−Ni(II) chelates, *J. Phys. Chem. B*, 2005, **109**(7), 2836.

46 G. Singh, S. Das Adhikary and D. Mandal, Physico- and electrochemical properties of first-row transition-metal-substituted sandwich polyoxometalates, *Inorg. Chem.*, 2023, **62**(22), 8551.

47 Q. Li, Q. Ding, W. Lin, J. Wang, M. Chen and M. Sun, Surface-enhanced Raman scattering of pyrazine on Au_5Al_5 bimetallic nanoclusters, *RSC Adv.*, 2017, **7**(20), 12170.

48 Y. Zhao, H. Wang and G. Wu, The charge shift in the excited virtual state of pyrimidine during the nonresonant Raman process at 632.8 nm: the bond polarizability study, *Spectrochim. Acta, Part A*, 2007, **66**(4), 1175.

49 Y. Shi, J. Li, B. Zhang, S. Lv, T. Wang and X. Liu, Tuning electronic structure of CoNi LDHs via surface Fe doping for achieving effective oxygen evolution reaction, *Appl. Surf. Sci.*, 2021, **565**, 150506.

50 H. J. Liu, S. Zhang, Y. M. Chai and B. Dong, Ligand modulation of active sites to promote cobalt-doped 1T-MoS_2 electrocatalytic hydrogen evolution in alkaline media, *Angew. Chem., Int. Ed.*, 2023, **135**(48), e202313845.

51 C.-J. Huang, H.-M. Xu, T.-Y. Shuai, Q.-N. Zhan, Z.-J. Zhang and G.-R. Li, Modulation strategies for the preparation of high-performance catalysts for urea oxidation reaction and their applications, *Small*, 2023, **19**(45), 2301130.

52 L. Zhang, L. Wang, H. Lin, Y. Liu, J. Ye, Y. Wen, A. Chen, L. Wang, F. Ni, Z. Zhou, *et al.*, A lattice-oxygen-involved reaction pathway to boost urea oxidation, *Angew. Chem., Int. Ed.*, 2019, **58**(47), 16820.

53 J. Hao, L. Yan, L. Luo, Q. Liu, Y. Bai, Y. Han, Y. Zhou, X. Zou and B. Xiang, Halogen chlorine triggered oxygen vacancy-rich $Ni(OH)_2$ with enhanced reaction kinetics for pseudocapacitive energy storage, *J. Energy Chem.*, 2023, **82**, 296.

54 D. Jia, H. Gao, W. Dong, S. Fan, R. Dang and G. Wang, Hierarchical α-$Ni(OH)_2$ composed of ultrathin nanosheets with controlled interlayer distances and their enhanced catalytic performance, *ACS Appl. Mater. Interfaces*, 2017, **9**(24), 20476.

55 J. Wang, M. Sun, X. Zhang, J. Liu, J. He, W. Ge, S. Kong, G. Zhang, M. Gao, Z. Sun and X. Shi, pH-dependent urea electrooxidation: from mechanism to catalysts and applications, *Adv. Mater.*, 2025, e15043.

